crystals

MDPI

Article

Core-Shell Structure and Dielectric Properties of $Ba_{0.6}Sr_{0.4}TiO_3$@ Fe_2O_3 Ceramics Prepared by Co-Precipitation Method

Zhuo Li [1,*], Chenbo Wang [1], Zixuan Wang [1], Dandan Zhang [1], Yangxiao Qin [1], Qiangbin Yang [1], Zhuo Wang [1], Peng Zhao [1], Xinshuai Ma [1], Minghan Li [1], Tao Ai [1], Xin Yan [1], Yanhui Niu [1], Biaolin Peng [2], Shikuan Sun [3] and Dawei Wang [4,*]

1 School of Materials Science and Engineering, Chang'an University, Xi'an 710061, China; 2019131005@chd.edu.cn (C.W.); 2020231039@chd.edu.cn (Z.W.); 2020231075@chd.edu.cn (D.Z.); 15129231922@163.com (Y.Q.); 2020231040@chd.edu.cn (Q.Y.); wangzhuo@chd.edu.cn (Z.W.); zyzhaop@chd.edu.cn (P.Z.); 2018902782@chd.edu.cn (X.M.); 2018901207@chd.edu.cn (M.L.); aitao@chd.edu.cn (T.A.); xinyan@chd.edu.cn (X.Y.); niuyh@chd.edu.cn (Y.N.)
2 School of Advanced Materials and Nanotechnology, Xidian University, Xi'an 710126, China; pengbl8@126.com
3 School of Material Science and Energy Engineering, Foshan University, Foshan 528000, China; Shikuansun@fosu.edu.cn
4 Shenzhen Institute of Advanced Electronic Materials, Shenzhen Institute of Advanced Technology, Chinese Academy of Sciences, Shenzhen 518055, China
* Correspondence: lizhuo@chd.edu.cn (Z.L.); wangdawei102@gmail.com (D.W.); Tel.: +86-29-8233-7340 (Z.L.)

Citation: Li, Z.; Wang, C.; Wang, Z.; Zhang, D.; Qin, Y.; Yang, Q.; Wang, Z.; Zhao, P.; Ma, X.; Li, M.; et al. Core-Shell Structure and Dielectric Properties of $Ba_{0.6}Sr_{0.4}TiO_3$@ Fe_2O_3 Ceramics Prepared by Co-Precipitation Method. *Crystals* **2021**, *11*, 623. https://doi.org/10.3390/cryst11060623

Academic Editors: Maria Gazda and Shujun Zhang

Received: 30 April 2021
Accepted: 27 May 2021
Published: 31 May 2021

Abstract: $Ba_{0.6}Sr_{0.4}TiO_3$ (BST) ceramic materials have been widely used in the field of multilayer ceramic capacitors. Surface modification through the surface coating to form a heterogeneous layer could effectively improve the dielectric properties. In this work, BST powders were prepared by a co-precipitation method. The effects of reaction conditions on the microstructure of the BST powder were investigated. The reaction temperatures significantly affected the morphology of BST powder, and the rhombic-type particles were obtained with the reaction temperature around 80 °C. Meanwhile, the BST@Fe_2O_3 was prepared by the chemical precipitation method using BST powders with rhombic-type microstructure as "core", and the so-called "core-shell" microstructure was confirmed in the BST@Fe_2O_3 powder. Then, BST@x wt%Fe_2O_3 (x = 2.5, 5, 7.5, and 10, denoting the different content of Fe_2O_3) ceramics were further prepared, and the influence of "core-shell" structure on the phase structure, microstructure, and dielectric properties was investigated. With the increasing of Fe_2O_3 content, the ferroelectric–paraelectric phase transition temperature shifts toward lower temperatures, and dielectric peaks gradually become broad and frequency-dependent, which may be due to inconsistent chemical composition from core to shell.

Keywords: $Ba_{0.6}Sr_{0.4}TiO_3$; co-precipitation; core-shell structure

1. Introduction

$Ba_{0.6}Sr_{0.4}TiO_3$ (BST) ceramic materials have been widely used in multilayer ceramic capacitors, infrared detectors, DRAM memories, and phased-array antenna, etc., due to their advantages of having a high dielectric constant, small dielectric loss, low leakage current, and large dielectric breakdown strength [1–7]. Many researchers have been focused on improving the dielectric properties of BST ceramics, such as doping, multiphase recombination, and surface modification. Among them, surface modification through the surface coating to form a heterogeneous coating layer has attracted attention extensively [8]. Tian [9] et al. found that $Ba_{0.75}Sr_{0.25}TiO_3$ powders coated with $Mg_{0.9}Zn_{0.1}O$ to form a "core-shell structure" could prevent the growth of BST particles in the processing of sintering and improve the dielectric tuning performance significantly. Wang et al. [10] found that $Ba_{0.6}Sr_{0.4}TiO_3$-$ZnNb_2O_6$ composites coated with Al_2O_3 as shell structure on the surface of BST powder can inhibit the formation of the second phase $BaNb_{3.6}O_{10}$ effectively,

which also improves the dielectric temperature performance dramatically. Zhang et al. [11] prepared $BaTiO_3$@SiO_2/PVDF composite and found that the breakdown strength was dramatically enhanced. Hence, constructing a "core-shell structure" with a different composition from the surface to the interior of the grain could improve the dielectric properties effectively. Besides that, it has already been confirmed that a "core-shell structure" can also improve magnetoelectric properties and photocatalytic activity. Reaz [12] et al. have successfully synthesized superior-quality $BaTiO_3$/iron oxide CSNP by the physiochemical synthesis process, and the observed superparamagnetic response due to the thin nanolayer of iron oxide has a wide variety of device applications. They also investigated the tunable magnetic properties of magneto-luminescent ZnO/iron oxide core-shell nanostructures using low-cost sonochemical synthesis [13]. Taufique et al. synthesized ZnO-CuO nanocomposites with improved photocatalytic activity for environmental and energy applications [14].

According to the previous studies, the "core-shell structure" can be influenced by the factors of the characteristics of coating ions and the preparation process. Kishi et al. [15] found that different coating ions have different diffusion rates in the solid solution, which could lead to the ununiform composition in the micro-area. Simultaneously, Kim et al. [16] found that the increase in milling time facilitated the shell formation leading to the increased shell portion in the core-shell grain.

Therefore, in this work, BST powder was prepared by the co-precipitation method, and then Fe_2O_3 was coated on the surface to form the $Ba_{0.6}Sr_{0.4}TiO_3$@Fe_2O_3 structure. The effects of reaction conditions on the microstructure and reaction mechanism were investigated. Besides, the influence of microstructure and composition on the dielectric properties for $Ba_{0.6}Sr_{0.4}TiO_3$@Fe_2O_3 ceramics was also studied.

2. Materials and Methods

2.1. Preparation of BST Powders

BST powders were prepared by the co-precipitation method according to the formula of $Ba_{0.6}Sr_{0.4}TiO_3$. Barium nitrate ($Ba(NO_3)_2$), strontium nitrate ($Sr(NO_3)_2$), and tetrabutyl titanate ($Ti(C_4H_9O)_4$) were used as raw materials, oxalic acid ($H_2C_2O_4$) as a precipitant and deionized water and ethanol as solvents. Firstly, an appropriate amount of $H_2C_2O_4$ was dissolved in the mixture of deionized water, and ethanol $Ti(C_4H_9O)_4$ was dissolved in ethanol. Secondly, these solutions were mixed, and ammonium hydroxide ($NH_3{\cdot}H_2O$) was added in the mixed solution drop by drop with continual stirring to keep the pH at 3 and finally formed the titanium oxalate ($H_2TiO(C_2O_4)_2$) solution. After that, $Ba(NO_3)_2$ and ($Sr(NO_3)_2$ were dissolved in deionized water at 80 °C, and then the mixture of $Ba(NO_3)_2$ and ($Sr(NO_3)_2$ was slowly added to the $H_2TiO(C_2O_4)_2$ solution with stirring continually at 80 °C for 2 h to obtain the BST precipitate. After aging for 24 h at room temperature, the precipitate was filtered, and the filtrate was collected and dried in an oven at 100 °C. Finally, the resulting precursor was calcined at 800 °C for 2 h to obtain the BST powders.

2.2. Preparation of BST@Fe_2O_3 Powders and Ceramics

The BST@x wt% Fe_2O_3 powders with x = 2.5, 5, 7.5, and 10 were obtained using the co-precipitation method. Firstly, the BST powders were dispersed in the mixture of deionized water and C_2H_5OH with ultrasonic vibration. The $Fe(NO_3)_3{\cdot}9H_2O$ with corresponding stoichiometric ratio were dissolved in the deionized water, stirred continuously, and then poured in the suspension of BST slowly. Secondly, $NH_3{\cdot}H_2O$ was added to the mixture drop by drop with continual stirring to control the pH between 9 and 10 [17] to obtain the precipitate BST@$Fe(OH)_3$. Finally, after centrifugally washed and dried in an oven at 100 °C, the powders were decomposed at 600 °C for 2 h to obtain BST@Fe_2O_3 powders. After that, the BST@Fe_2O_3 powders were mixed with 6% PVA and pressed into pellets of 12 mm diameter and 1 mm thickness by uniaxial pressing. These pellets were sintered in air at 1200 °C for 2 h.

2.3. Characterization

The phase structure of powders and sintered pellets were investigated by X-ray diffraction (XRD; D8 Advance, Bruker AXS, Billerica, MA, USA) operated at 40 kV with CuKa1 radiation (k = 0.15406 nm) and 2θ range from 20 to 90 degree. The microstructures of the powder and sintered pellets were observed by field-emission scanning electron microscopy (FE-SEM; S-4800, Hitachi, Tokyo, Japan). The core-shell structure and elemental compositions were detected by transmission electron microscopy (TEM; JEM-200CX, Hitachi) equipped with energy-dispersive X-ray spectroscopy (EDS; FeatureMax, Oxford Instruments, Abingdon, UK) operated at 200 kV. Fourier-transform infrared spectra were obtained using a Bruker Tensor-II FT-IR spectrometer (FTIR; Tensor27, Bruker Germany, Berlin, Germany). Differential scanning calorimetry (DSC) and thermogravimetric analysis (TGA) were carried out using a synchronous thermal analyzer (SDT-Q600, TA Instruments Inc., New Castle, DE, USA) with nitrogen flow (50 mL/min) over a temperature range of 30–1000 °C and at a heating rate of 10 °C/min.

For measuring the electrical properties, silver electrode paste was applied on both surfaces of the sintered pellets followed by firing at 550 °C for 30 min. The dielectric characteristics were measured by an impedance analyzer (Agilent 4294 A) at a frequency range of 1 kHz to 1 MHz at −150 °C–200 °C.

3. Results and Discussion

3.1. TGA-DSC Analysis of BST Precursor Prepared by Co-Precipitation

Figure 1 shows the TGA and DSC curves of the BST precursor prepared by the co-precipitation method. From the TGA curve, it can be observed that the actual weight loss of the BST powder was 48%, which is well-matched with the theoretical weight loss of 49%. From the DSC curve, it was obvious that the physically absorbed water of $Ba_{1-x}Sr_xTiO(C_2O_4)_2{\cdot}4H_2O$ removed from 25 °C to 240 °C, corresponding to an exothermic peak at 101 °C and $Ba_{1-x}Sr_xTiO(C_2O_4)_2$, decomposed to form $Ba_{1-x}Sr_xCO_3$ and TiO_2 at 240 °C to 470 °C, accompanied by an exothermic peak at 337 °C. Meanwhile, $Ba_{1-x}Sr_xCO_3$ and TiO_2 diffused with each other to form $Ba_{0.6}Sr_{0.4}TiO_3$ at 470 °C to 700 °C, along with an exothermic peak at 584 °C. Up to 730 °C and above, the pure phase BST powder was produced. Therefore, the preparation of $Ba_{0.6}Sr_{0.4}TiO_3$ required the following reactions:

$$(C_4H_9O)_4Ti + 4H_2O \rightarrow Ti(OH)_4\downarrow + C_4H_9OH \quad (1)$$

$$Ti(OH)_4 + 2H_2C_2O_4 \rightarrow H_2TiO(C_2O_4)_2 \quad (2)$$

$$H_2TiO(C_2O_4)_2 + xSr(NO_3)_2 + (1-x)Ba(NO_3)_2 + 4H_2O \rightarrow Ba_{1-x}Sr_xTiO(C_2O_4)_2{\cdot}4H_2O + 4HNO_3 \quad (3)$$

$$Ba_{1-x}Sr_xTiO(C_2O_4)_2{\cdot}4H_2O \rightarrow Ba_{1-x}Sr_xTiO(C_2O_4)_2 + 4H_2O \quad (4)$$

$$Ba_{1-x}Sr_xTiO(C_2O_4)_2 \rightarrow Ba_{1-x}Sr_xCO_3 + TiO_2 + 2CO_2\uparrow + 2CO\uparrow \quad (5)$$

$$Ba_{1-x}Sr_xCO_3 + TiO_2 \rightarrow Ba_{1-x}Sr_xTiO_3 + CO_2\uparrow \quad (6)$$

3.2. Effect of Calcining Temperature on IR Transmittance Spectra and Microstructure of BST

In order to further confirm the reaction mechanism of BST powder, the infrared spectra of BST precursor dried at 100 °C, calcined at 500 °C and 800 °C were measured respectively, as shown in Figure 2. It can be seen that the absorption peaks of 2332 cm^{-1}, 1397 $cm^{-1,}$ and 875 cm^{-1} corresponded to the stretching vibration of CO_2 and carbonate, indicating that the BST precursor powder decomposes into carbonate, which is in agreement with Equation (5). The absorption peak of 507 cm^{-1} corresponds to the stretching vibration of Ti-O, suggesting that the pure phase BST powder is formed after calcination at 800 °C.

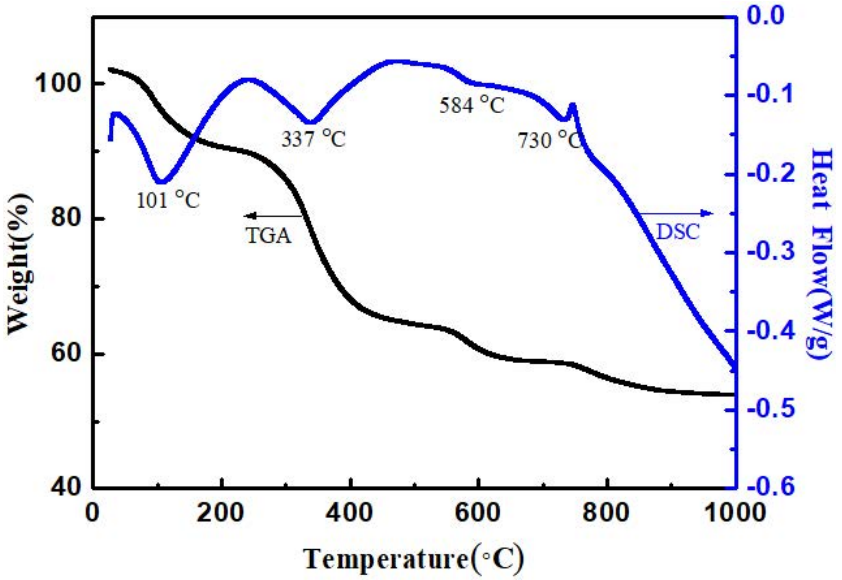

Figure 1. TGA-DSC curves of BST precursors prepared by co-precipitation method.

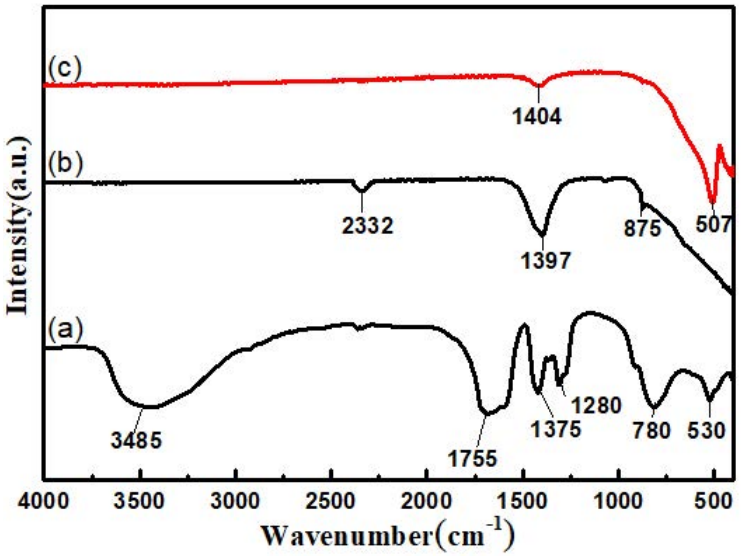

Figure 2. The FT-IR spectra of BST precursors (**a**) dried at 100 °C and calcined at (**b**) 500 °C and (**c**) 800 °C, respectively.

Figure 3 shows the XRD pattern and SEM images of BST powders calcined at 800 °C for 2 h. All the major diffraction peaks in the XRD pattern could be indexed according to the BST perovskite phase, and no secondary phase could be detected, indicating that a solid solution had been formed (Figure 3a). SEM images show a rhombic hexahedron growth with fusiform-type grains composed of a number of tiny sub-round particles, as shown in Figure 3b,c. Generally, the reaction conditions in the co-precipitation process significantly influence the morphology of the final powder, such as the addition of different polymeric dispersants [18], the emission of gases during the pyrolysis process, and using $C_2O_4^{2-}$ as the capping agent could make anisotropic crystal growth [19]. According to the growth mechanism of the crystal, the high reaction temperature contributes to the more uniform surface energy of each lattice plane, leading to the rhombic hexahedron crystal growth followed by secondary nucleation on the crystal surface, eventually forming poly-crystalline particles with sizes ranging from 0.3 to 1.6 μm [20].

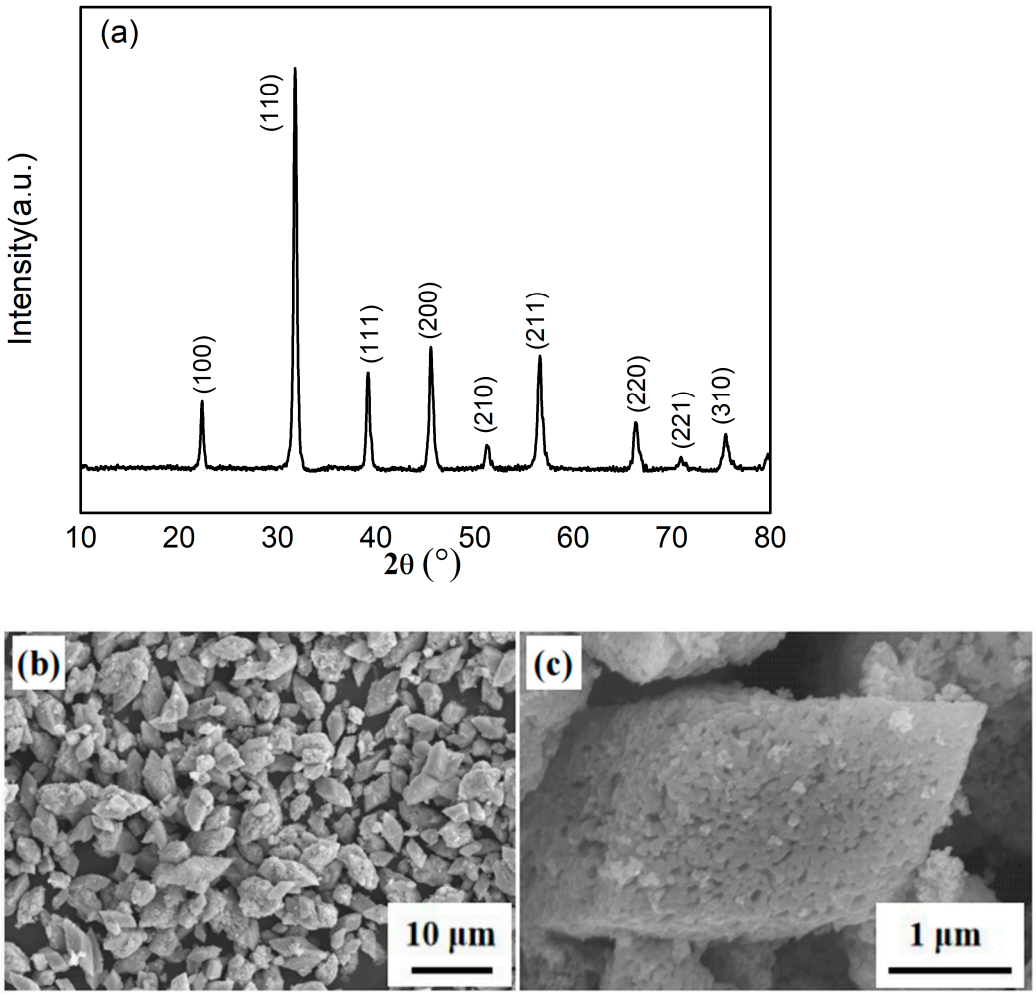

Figure 3. (**a**) The XRD spectrum, (**b**) SEM, and (**c**) partial enlarged SEM image of BST precursors calcined at 800 °C for 2 h.

3.3. Effect of Fe_2O_3 Coating on the Microstructure of BST@Fe_2O_3 Composite Powders

Figure 4 shows the XRD spectra with peak intensity in log scale of BST@Fe_2O_3 composite powders with different Fe_2O_3 coating amounts calcined at 600 °C for 2 h [21]. It was clear that the main phase structure was still perovskite $Ba_{0.6}Sr_{0.4}TiO_3$ in the samples (PDF#34-0411). When the coating content of Fe_2O_3 was lower than 5 wt%, it was difficult to detect the diffraction peaks of Fe_2O_3. When the coating content of Fe_2O_3 was more than 5 wt%, the second phase Fe_2O_3 corresponding to diffraction peaks of 2θ = 24.2°, 33.2°, 35.7° was apparent (PDF#85-0599), and the intensity of the diffraction peaks increased with the amount of Fe_2O_3 [22].

The effect of coating on the microstructure of BST was studied, which is shown in the SEM images of BST and BST@ 10% Fe_2O_3 powders (Figure 5). Compared to the pure BST powder with regular morphology, clear edges, and smooth surface (Figure 5c), the encapsulated BST@Fe_2O_3 powder had obvious flocculent particles deposited on its surface, and the blurred edges, as shown in Figure 5d.

The TEM associated with the EDS was further employed to further investigate the microstructure of BST@ 10 wt% Fe_2O_3, as shown in Figures 6 and 7, respectively. The BST particles were surrounded with a large number of flocculent crystalline particles, displaying an overall uniform cohesive coating layer with a size ranging from about dozens to 100 nm (Figure 6). The relevant EDS spectra associated with elemental mapping show that the Fe element is enriched in the edge (Figure 7), indicating that the "core-shell" structure was well-formed.

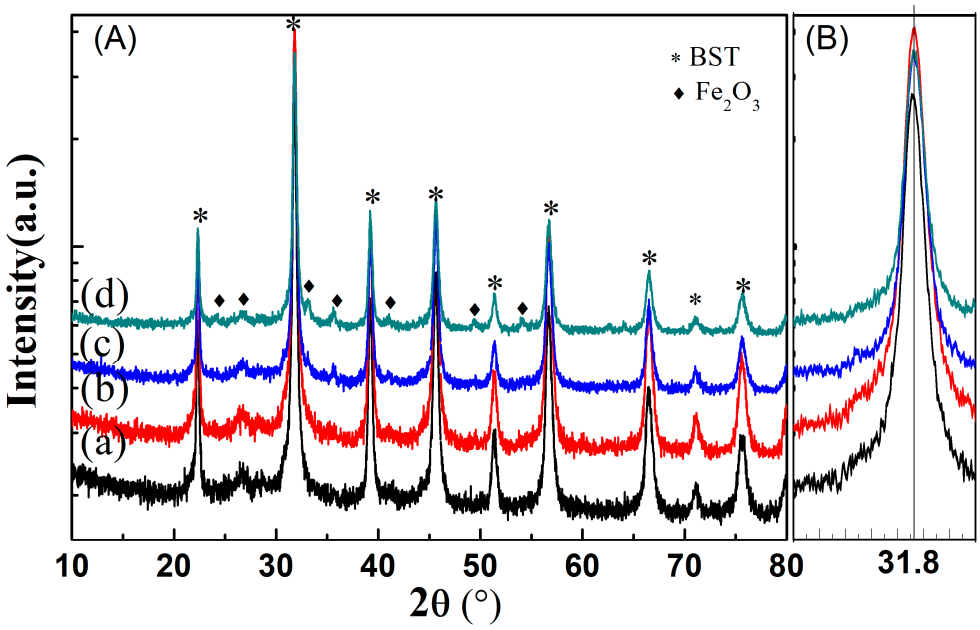

Figure 4. (**A**) XRD patterns of BST@Fe_2O_3 composite powders with different Fe_2O_3 coating amounts (**a**) 2.5 wt%, (**b**) 5 wt%, (**c**) 7.5 wt% and (**d**) 10 wt% calcined at 600 °C for 2 h. (**B**) the locally magnified (110) diffraction peaks.

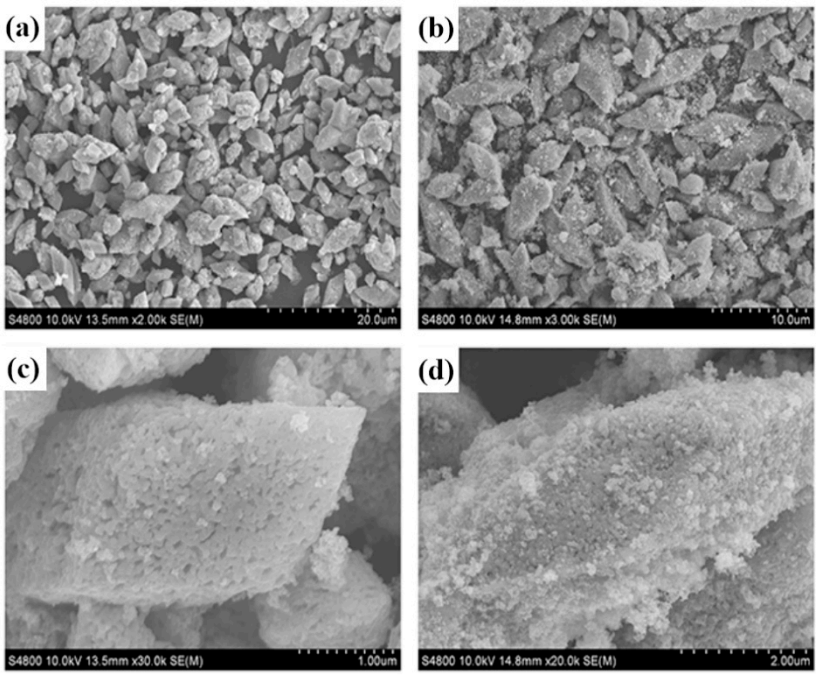

Figure 5. SEM images of (**a**,**c**) pure phase BST and (**b**,**d**) BST@ 10 wt% Fe_2O_3.

3.4. BST@Fe_2O_3 Composite Ceramics: Microstructure

Figure 8 shows the XRD spectra of BST@Fe_2O_3 ceramics sintered at 1200 °C for 2 h. It was evident that with an increase of Fe_2O_3, the second phase emerged in the form of $Ba_2(Fe_2Ti_4O_{13})$ (PDF#87-1480), which indicated that the high sintered temperature encourages the reaction between Fe_2O_3 and BST perovskite phase to form the $Ba_2(Fe_2Ti_4O_{13})$ phase. Figure 9 shows the surface morphology of BST@Fe_2O_3 ceramics with different Fe_2O_3 content. The microstructure of BST@Fe_2O_3 ceramics displayed a relatively uniform grain size, but poor density was clear, as shown in Figure 9. In general, a big gap would generate between rhombic-type grains [23–27], which would lead to the migration of grain

boundary being more difficult, followed by the appetence of pores in the ceramics. Besides that, Fe_2O_3 coated on the surface of BST would inhibit the migration of grain boundary in the processing of sintering, thus leading to reduced grain size and density [28].

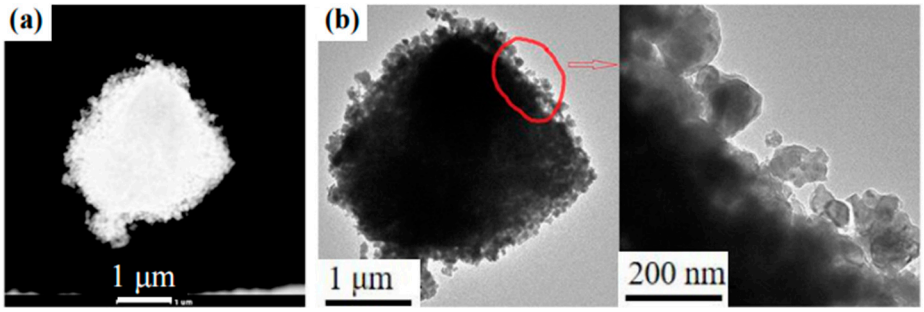

Figure 6. TEM images in (**a**) low magnification and (**b**) high magnification for the BST@ 10 wt% Fe_2O_3 particle and the partially enlarged view of BST@ 10 wt% Fe_2O_3.

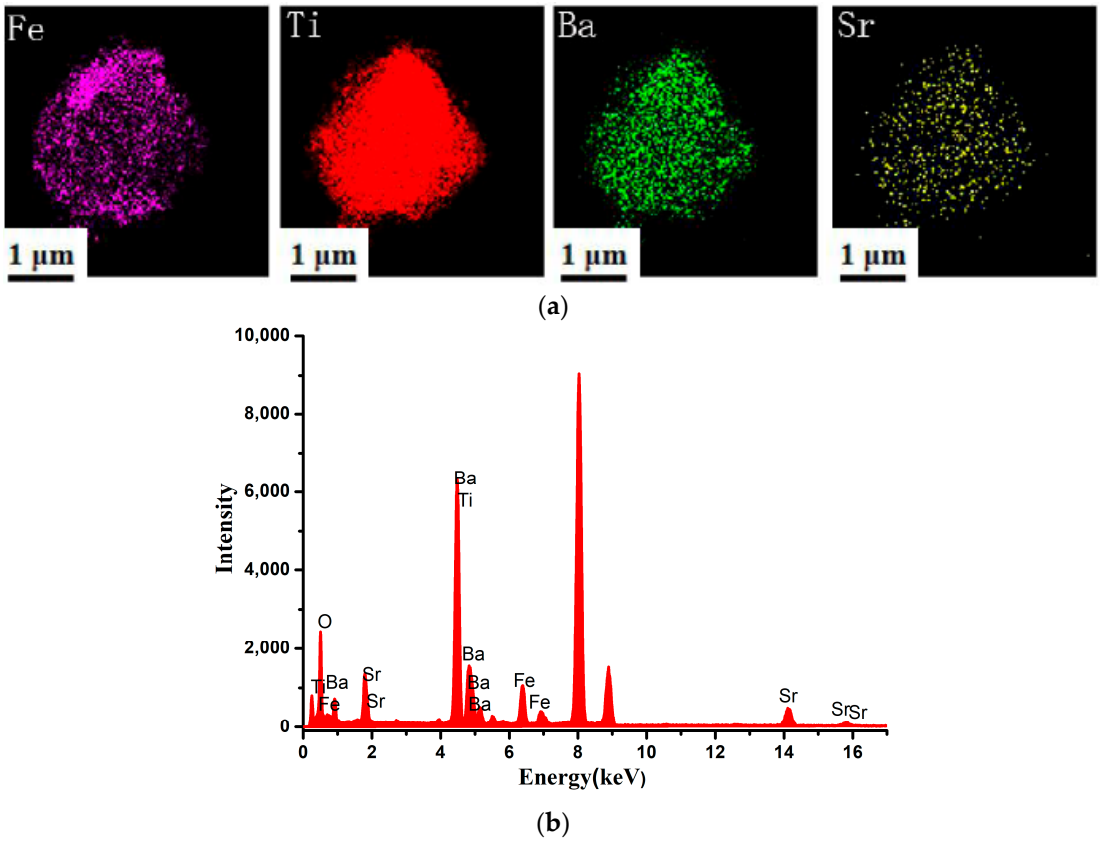

Figure 7. (**a**) Surface scanning elemental distribution and (**b**) EDS results of BST@ 10wt% Fe_2O_3.

3.5. BST@Fe_2O_3 Ceramics: Dielectric Properties

To investigate the effect of coating on the dielectric properties of BST ceramics, the temperature dependence from −150 °C to 200 °C of the dielectric constant ε′ (T) and the loss tangent tan δ(T) for different BST@Fe_2O_3 ceramics is plotted in Figure 10 under various measurement frequencies from 1 kHz to 1 MHz. Obviously, with the increase of Fe_2O_3 content, the dielectric peaks of the ferroelectric–paraelectric phase transition shifted toward low temperatures from 11 °C for pure BST to −49 °C for BST@7.5%wt Fe_2O_3 ceramics. Ferroelectric–paraelectric phase transition peaks also gradually became broad and frequency-dependent, which was probably due to the particular "core-shell"

structure of BST@Fe_2O_3. The so-called "core-shell" structure makes it difficult for Fe^{3+} to diffuse into the core of BST, thus resulting in inconsistent chemical composition from core to shell, which leads to the broaden and dispersive ferroelectric-paraelectric phase transition. In addition, dielectric constant ε′ obtained a maximum at 7.5 wt% Fe_2O_3, which could be explained by the grain size effects, clearly seen in Figure 9a–d. Previous reports have proved that the reduced grain size in slightly Fe_2O_3 doped BST ceramics resulted in the reduction of dielectric properties and broadening of the dielectric peak [29]. While for the ceramics with 10 wt% Fe_2O_3, the dielectric properties drop at all, which may be due to the combination of impurity and lower density (Figure 9e). Except that, as a whole, the tan δ increased with increasing Fe_2O_3 content. The tan δ also decreased with the increase in frequency.

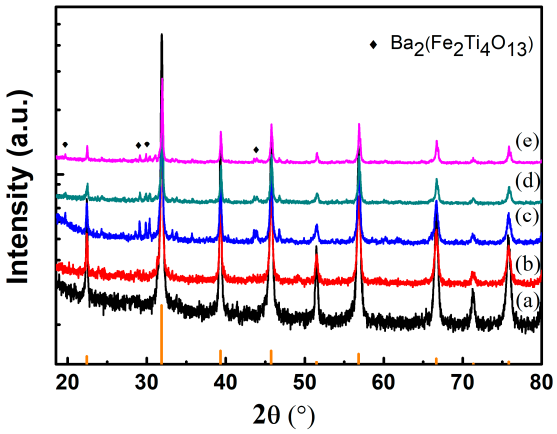

Figure 8. XRD patterns of BST@Fe_2O_3 ceramics with different coating amounts (**a**) 0 wt%, (**b**) 2.5 wt%, (**c**) 5 wt%, (**d**) 7.5 wt%, and (**e**) 10 wt%.

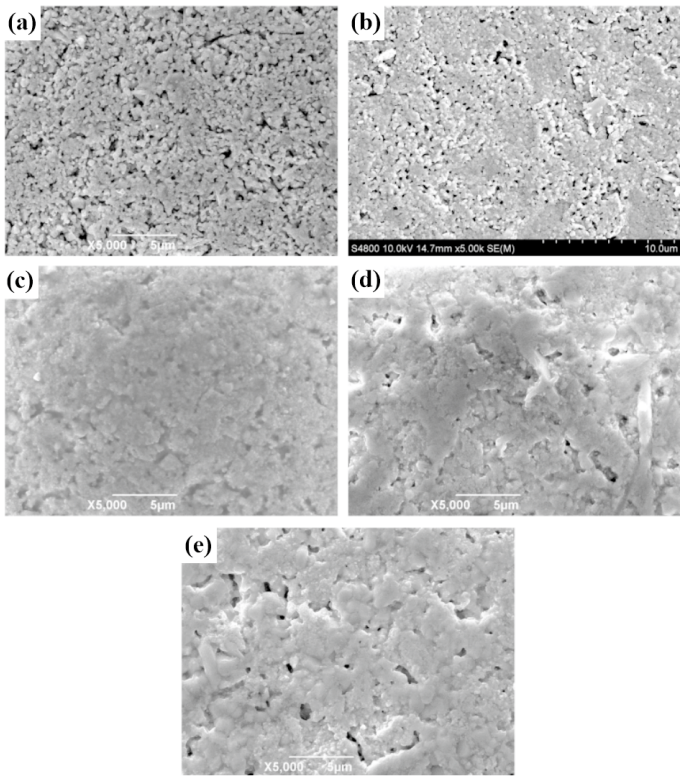

Figure 9. The surface microstructure of the BST@Fe_2O_3 ceramics with different coating amounts (**a**) 0 wt%, (**b**) 2.5 wt%, (**c**) 5 wt%, (**d**) 7.5 wt%, and (**e**) 10 wt%.

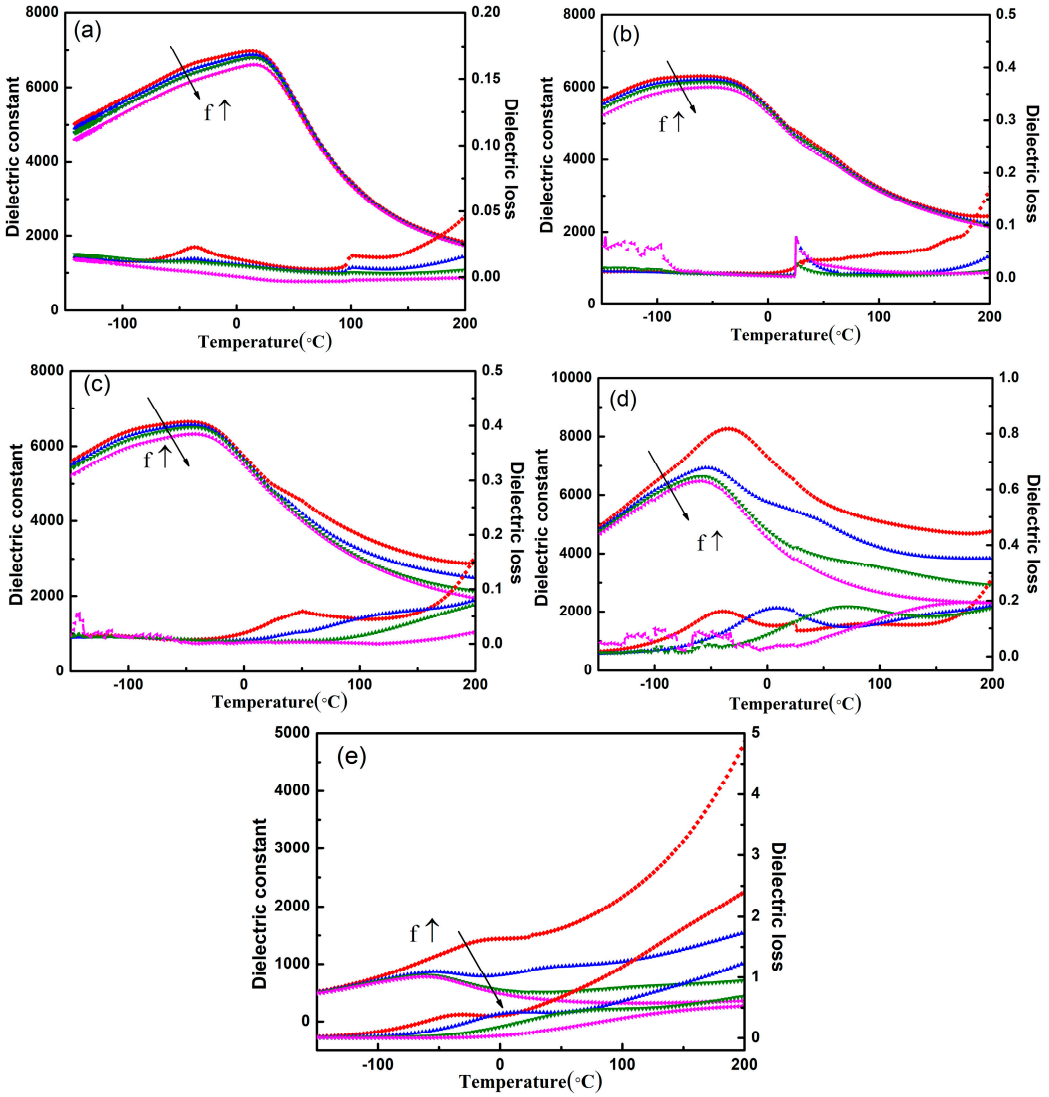

Figure 10. Temperature dependence of dielectric permittivity ε′ and dielectric loss tan δ for the BST@Fe_2O_3 ceramics with different coating amounts (**a**) 0 wt%, (**b**) 2.5 wt%, (**c**) 5 wt%, (**d**) 7.5 wt%, and (**e**) 10 wt% from 1 kHz to 1 MHz.

4. Conclusions

In this work, the BST and BST@Fe_2O_3 powders were successfully prepared by the co-precipitation method. The reaction temperatures had a significant effect on the morphology of the BST powder. As the reaction temperature around 80 °C, the rhombic-type particles were obtained, which were suitable to serve as the "core" and the so-called "core-shell" microstructure, as confirmed in the BST@Fe_2O_3 powders. In addition, BST@x wt%Fe_2O_3 ceramics were further prepared, and the influence of "core-shell" structure on the phase structure, microstructure, and dielectric properties was investigated. The results showed that with the increasing of Fe_2O_3 content, the ferroelectric–paraelectric phase transition temperature shifts toward lower temperatures, and due to the inconsistent chemical composition from core to shell, dielectric peaks gradually become broad and frequency-dependent.

Author Contributions: Analysis and writing, Z.L. and Z.W. (Zixuan Wang); experiments and characterization, C.W., Y.Q., D.Z., X.M., M.L. and Q.Y.; project administration, Z.W. (Zhuo Wang) and Y.N.; conceptualization and methodology, P.Z., T.A., X.Y., B.P., S.S. and D.W. All authors have read and agreed to the published version of the manuscript.

Funding: This research was funded by the National Natural Science Foundations of China (Grant No. 11604022), Natural Science Foundation of Shaanxi province, China (2021JM-172) and the Fundamental Research Funds for the Central Universities, CHD (Nos. 300102311404 and 300102310301).

Institutional Review Board Statement: Not applicable.

Informed Consent Statement: Not applicable.

Acknowledgments: The authors thank the financial support of the National Natural Science Foundations of China (Grant No. 11604022), Natural Science Foundation of Shaanxi province, China (2021JM-172) and the Fundamental Research Funds for the Central Universities, CHD (Nos. 300102311404 and 300102310301).

Conflicts of Interest: The authors declare no conflict of interest.

References

1. Tagantsev, A.K.; Sherman, V.O.; Astafiev, K.F.; Venkatesh, J.; Setter, N. Ferroelectric materials for microwave tunable applications. *J. Electroceramics* **2003**, *11*, 5–66. [CrossRef]
2. Kaminow, I. Principles and Applications of Ferroelectrics and Related Materials. *Phys. Today* **1978**, *31*, 56–58.
3. Yu, P.; Cui, B.; Shi, Q. Preparation and characterization of $BaTiO_3$ powders and ceramics by sol–gel process using oleic acid as surfactant. *Mater. Sci. Eng. A* **2008**, *473*, 34–41. [CrossRef]
4. Ezhilvalavan, S.; Tseng, T.Y. Progress in the developments of (Ba, Sr) TiO_3 (BST) thin films for Gigabit era DRAMs. *Mater. Chem. Phys.* **2000**, *65*, 227–248. [CrossRef]
5. Carlson, C.M.; Rivkin, T.V.; Parilla, P.A.; Perkins, J.D.; Ginley, D.S.; Kozyrev, A.B.; Oschadchy, V.N.; Pavlov, A.S. Large dielectric constant ($\varepsilon/\varepsilon_0 > 6000$) $Ba_{0.4}Sr_{0.6}TiO_3$ thin films for high-performance microwave phase shifters. *Appl. Phys. Lett.* **2000**, *76*, 1920–1922. [CrossRef]
6. Fournaud, B.; Rossignol, S.; Tatibou, J.M.; Tholomb, S. Spherical pellets of $BaTiO_3$ and $Ba_{0.67}Sr_{0.33}TiO_3$ perovskite-type compounds made by a sol–gel oil drop process for non-thermal plasma applications. *Mater. Process. Technol.* **2009**, *209*, 2515–2521. [CrossRef]
7. Ćirković, J.; Vojisavljević, K.; Nikolić, N.; Vulić, P.; Branković, Z.; Srećković, T.; Branković, G. Dielectric and ferroelectric properties of BST ceramics obtained by a hydrothermally assisted complex polymerization method. *Ceram. Int.* **2015**, *41*, 11306–11313. [CrossRef]
8. Kim, C.-H.; Park, K.-J.; Yoon, Y.-J.; Hong, M.-H.; Hong, J.-O.; Hur, K.-H. Role of Yttrium and Magnesium in the Formation of Core-shell Structure of $BaTiO_3$ Grains in MLCC. *J. Eur. Ceram. Soc.* **2008**, *28*, 1213–1219. [CrossRef]
9. Tian, H.; Qi, J.; Wang, Y.; Chan, H.; Choy, C. Improved Dielectric Properties of BaxSr1−$xTiO_3$ Based Composite Ceramics Derived from Core-shell Structured Nanopowders. *Prog. Solid State Chem.* **2005**, *33*, 207–215. [CrossRef]
10. Wang, T.; Gao, F.; Hu, G.; Tian, C. Synthesis $Ba_{0.6}Sr_{0.4}TiO_3$-$ZnNb_2O_6$, Composite Ceramics Using Chemical Coating Method. *J. Alloys Compd.* **2010**, *504*, 362–366. [CrossRef]
11. Zhang, Z.; Gu, Y.; Bi, J.; Wang, S.; Li, M.; Zhang, Z. Tunable BT@SiO_2, Core@shell Filler Reinforced Polymer Composite with High Breakdown Strength and Release Energy Density. *Compos. Part A Appl. Sci. Manuf.* **2016**, *85*, 172–180. [CrossRef]
12. Reaz, M.; Haque, A.; Ghosh, K. Synthesis, Characterization, and Optimization of Magnetoelectric $BaTiO_3$–Iron Oxide Core–Shell Nanoparticles. *Nanomaterials* **2020**, *10*, 563. [CrossRef] [PubMed]
13. Reaz, M.; Haque, A.; Cornelison, D.M.; Wanekaya, A.; Delong, R.; Ghosh, K. Magneto-luminescent zinc/iron oxide core-shell nanoparticles with tunable magnetic properties. *Phys. E Low-Dimens. Syst. Nanostruct.* **2020**, *123*, 114090. [CrossRef]
14. Taufique, M.F.N.; Haque, A.; Karnati, P.; Ghosh, K. ZnO–CuO nanocomposites with improved photocatalytic activity for environmental and energy applications. *J. Electron. Mater.* **2018**, *47*, 6731–6745. [CrossRef]
15. Kishi, H.; Okino, Y.; Honda, M.; Iguchi, Y.; Imaeda, M.; Takahashi, Y.; Ohsato, H.; Okuda, T. The Effect of MgO and Rare-Earth Oxide on Formation Behavior of Core-Shell Structure in $BaTiO_3$. *Jpn. J. Appl. Phys.* **1997**, *36*, 5954–5957. [CrossRef]
16. Kim, C.-H.; Park, K.-J.; Yoon, Y.-J.; Sinn, D.-S.; Kim, Y.-T.; Hur, K.-H. Effects of Milling Condition on the Formation of Core–shell Structure in $BaTiO_3$ Grains. *J. Eur. Ceram. Soc.* **2008**, *28*, 2589–2596. [CrossRef]
17. Schrey, F. Effect of pH on the Chemical Preparation of BariumStrontium Titanate. *J. Am. Ceram. Soc.* **2010**, *48*, 401–405. [CrossRef]
18. Li, M.L.; Xu, M.X. Effect of Dispersant on Preparation of Barium Strontium Titanate Powders through Oxalate Co-precipitation Method. *Mater. Res. Bull.* **2009**, *44*, 937–942. [CrossRef]
19. Khollam, Y.; Deshpande, S.; Potdar, H.; Bhoraskar, S.; Sainkar, S.; Date, S. Simple Oxalate Precursor Route for the Preparation of Barium Strontium Titanate: Ba1−x$SrxTiO_3$ Powders. *Mater. Charact.* **2005**, *54*, 63–74. [CrossRef]
20. Testino, A.; Buscaglia, M.T.; Buscaglia, V.; Viviani, M.; Bottino, C.; Nanni, P. Kinetics and Mechanism of Aqueous Chemical Synthesis of $BaTiO_3$ Particles. *Chem. Mater.* **2004**, *16*, 1536–1543. [CrossRef]
21. Mamun, M.A.A.; Haque, A.; Pelton, A.; Paul, B.; Ghosh, K. Structural, Electronic, and Magnetic Analysis and Device Characterization of Ferroelectric–Ferromagnetic Heterostructure (BZT–BCT/LSMO/LAO) Devices for Multiferroic Applications. *IEEE Trans. Magn.* **2018**, *54*, 1–8. [CrossRef]
22. Mahani, R.; Battisha, I.; Aly, M.; Abou-Hamad, A. Structure and dielectric behavior of nano-structure ferroelectric BaxSr1−xTiO3 prepared by sol-gel method. *J. Alloys Compd.* **2010**, *508*, 354–358. [CrossRef]

23. Wang, D.; Fan, Z.; Rao, G.; Wang, G.; Liu, Y.; Yuan, C.; Ma, T.; Li, D.; Tan, X.; Lu, Z.; et al. Ultrahigh piezoelectricity in lead-free piezoceramics by synergistic design. *Nano Energy* **2020**, *76*, 104944. [CrossRef]
24. Lai, X.; Hao, H.; Liu, Z.; Li, S.; Liu, Y.; Emmanuel, M.; Yao, Z.; Cao, M.; Wang, D.; Liu, H. Structure and Dielectric Properties of MgO Coated $BaTiO_3$ Ceramics. *J. Mater. Sci. Mater. Electron.* **2020**, *31*, 8963–8970. [CrossRef]
25. Han, D.; Wang, C.; Lu, D.; Hussain, F.; Wang, D.; Meng, F. A temperature stable $(Ba_{1-x}Ce_x)(Ti_{1-x/2}Mg_{x/2})O_3$ lead-free ceramic for X4D capacitors. *J. Alloys Compd.* **2020**, *821*, 153480. [CrossRef]
26. Sun, H.; Duan, S.; Liu, X.; Wang, D.; Sui, H. Lead-free $Ba_{0.98}Ca_{0.02}Zr_{0.02}Ti_{0.98}O_3$ ceramics with enhanced electrical performance by modifying MnO_2 doping content and sintering temperature. *J. Alloys Compd.* **2016**, *670*, 262–267. [CrossRef]
27. Wang, Z.; Wang, X.; Chao, X.; Wei, L.; Yang, B.; Wang, D.; Yang, Z. Synthesis, structure, dielectric, piezoelectric, and energy storage performance of $(Ba_{0.85}Ca_{0.15})(Ti_{0.9}Zr_{0.1})O_3$ ceramics prepared by different methods. *J. Mater. Sci. Mater. Electron.* **2016**, *27*, 5047–5058. [CrossRef]
28. Amos, K.; Marzio, F.D. Characterization of doped BST thin films deposited by sol-gel for tunable microwave devices. *IEEE Trans. Ultrason. Ferroelectr. Freq. Control* **2010**, *57*, 1029.
29. Herner, S.B.; Selmi, F.A.; Varadan, V.V.; Varadan, V.K. The effect of various dopants on the dielectric properties of barium strontium titanate. *Mater. Lett.* **1993**, *15*, 317–324. [CrossRef]